

Design of a Rotational Hydroelastic Actuator for a Powered Exoskeleton for Upper Limb Rehabilitation

Arno H. A. Stienen*, Edsko E. G. Hekman, Huub ter Braak, Arthur M. M. Aalsma, Frans C. T. van der Helm, and Herman van der Kooij

Abstract—The goal of this study was to validate the suitability of a novel rotational hydroelastic actuator (rHEA) for use in our new rehabilitation exoskeleton for the upper limbs, the Limbact. The rHEA consists of a rotational hydraulic actuator and a custom-designed symmetric torsion spring in a series-elastic configuration. For rehabilitation therapy and impairment quantification, both compliant impedance control and stiff admittance control modes are possible. In the validation experiments, the torque bandwidth of the rHEA was limited to 18 Hz for a desired 20 N·m reference signal (multisine, constant spectrum) due to the transport delays in the long flexible tubes between the valve and cylinder. These transport delays also required changes to existing theoretical models to better fit the models on the measured frequency response functions. The (theoretical) measurable torque resolution was better than 0.01 N·m and the (validated) delivered torque resolution below 1 N·m. After the validation experiments, further iterative improvements resulted in a spring design capable of a maximum output torque of 50 N·m with an intrinsic stiffness of 150 N·m/rad and a slightly higher bandwidth. With the design locked, the maximum measurable isometric torque is 100 N·m. In conclusion, the rHEA is suitable for upper limb rehabilitation therapy as it matches the desired performance.

Index Terms—Actuator design, rehabilitation robotics, stroke rehabilitation, upper extremities.

I. INTRODUCTION

PATIENT-FRIENDLY robots are used as diagnostic and therapeutic aids in upper limb rehabilitation. Through physical manipulation of the arm and usage of virtual environments, innovative interaction schemes are explored in search of the best possible therapy. Robot-assisted therapy is considered to be as good or better than conventional therapy [1]–[4], more challenging for the patients, and less la-

bor intensive for the therapists. It also provides physicians, therapists, and the scientific community with more objectively gathered data on impairment quantification before, during, and after therapy.

Systematic reviews on nonrobot-assisted therapy for the upper extremities indicate that intensive and task-specific exercises consisting of repetitive movements with active patient participation give the best results [5]–[9]. With the Freebal [10] and Dampace [11], we created two passive devices for rehabilitation therapy. The Freebal is a cable-suspension system that supports the arm against gravity. The Dampace is a self-aligning exoskeleton that actively controls resistance torques on the shoulder and elbow joints. Both can be used for intensive, repetitive, and task-specific exercises. As passive devices, they force the patients to actively participate.

However, passive devices are not always appropriate for all types of therapy or the quantification of impairments. For example, with an active device, it is possible to provide assist as needed [12] and create more realistic virtual environments [13]. To separate and quantify intrinsic and reflexive components of human arm dynamics [14]–[16], active arm perturbation is needed to trigger the human system. Therefore, we developed a new exoskeleton, similar in design to the passive Dampace, but to be fitted with active actuators.

In the lower extremity powered exoskeleton (LOPES) project for the lower extremities [17], series elastic actuation (SEA) [18], [19] made high-compliant impedance control possible despite high and highly variable friction forces in the Bowden cables [20]–[22]. Compared to electromotors with large gearbox reductions, SEA has low output impedance and good back-drivability, force control, and output resolution, at the cost of maximum actuator stiffness and force bandwidth. Compared to high-compliant pneumatic actuation, SEA has a much higher force bandwidth and output resolution. SEA does not require a perfect actuator model because it is controlled solely on the deflection of the elastic element, and this spring deflection is a direct measure for the applied force. Measuring it at the end of the force chain allows the SEA controller to reject most of the system noise, nonlinearities, and other interfering dynamics entered earlier in the chain. These properties make SEA a good choice for actuation of our powered exoskeleton for the upper limbs. Therefore, the goal of this study is to validate the suitability of a new SEA actuator for stroke rehabilitation therapy and impairment quantification with the new Limbact rehabilitation exoskeleton (see Fig. 1). In this paper, the rotational hydroelastic actuator (rHEA) design and theoretical

Manuscript received December 7, 2008; revised February 9, 2009. First published April 7, 2009; current version published February 17, 2010. This work was supported by SenterNovem (NL) under Grant TSGE2050. Asterisk indicates corresponding author.

*A. H. A. Stienen is with the Laboratory for Biomechanical Engineering, University of Twente, Drienerlolaan 5, 7500 AE Enschede, The Netherlands, and also with the Department of Physical Therapy and Human Movement Sciences, Northwestern University, Chicago, IL 60611 USA (e-mail: arnostienen@gmail.com).

E. E. G. Hekman is with the Laboratory for Biomechanical Engineering, University of Twente, Drienerlolaan 5, 7500 AE Enschede, The Netherlands (e-mail: e.e.g.hekman@utwente.nl).

H. ter Braak and A. M. M. Aalsma are with BAAT Medical, Twekkelerweg 263, 7553 LZ Hengelo (OV), The Netherlands (e-mail: huub@baatmedical.com; arthur@baatmedical.com).

F. C. T. van der Helm and H. van der Kooij are with the Laboratory for Biomechanical Engineering, University of Twente, Drienerlolaan 5, 7500 AE Enschede, The Netherlands, and also with the Department of Biomechanical Engineering, Delft University of Technology, Mekelweg 2, 2628 CD Delft, The Netherlands (e-mail: f.c.t.vanderhelm@tudelft.nl; h.vanderkooij@utwente.nl).

Digital Object Identifier 10.1109/TBME.2009.2018628

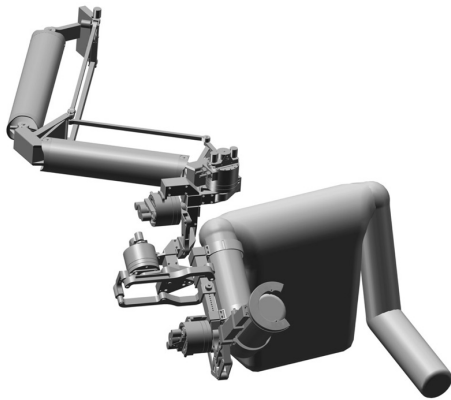


Fig. 1. Design of the upcoming torque-driven exoskeleton, the Limbact. The mechanical design is similar to the passive and self-aligning Dampace, but it has active actuation on all shoulder and elbow axes.

control model are described in detail and their performance is experimentally validated.

A preliminary version of this paper has appeared at IEEE Biorob 2008 [23].

II. DESIGN

A. Requirements

The SEA should weigh less than 1.5 kg and be smaller than $100 \times 100 \times 100$ mm to be directly mountable on an exoskeleton. Weight support of the arm and exoskeleton requires a high maximum torque with low bandwidth. Conventional therapy exercises and simple virtual environments require lower maximum torques and human system identification requires a higher bandwidth. Therefore, the high-force bandwidth (50 N·m) should be above 5 Hz and the low-force bandwidth (5 N·m) should be above 20 Hz. The delivered torque resolution should be at least below 1 N·m—which we found to be the level just distinguishable by most healthy subjects and stroke patients with the Dampace—but preferably be as low as possible. The measured torque resolution should be below 0.1 N·m. The minimal impedance—the torque felt when moving the actuator while no torque is requested—is preferably as low as possible. Isometric torques need to be measured at up to 100 N·m but additional mechanisms may be used to make this possible. These requirements were specified with the help of multiple physicians, therapists, and human movement scientists from The Netherlands.

B. Overall Design

Space and weight requirements for use on an exoskeleton immediately lead to a compact, rotational design for the SEA.

For actuation of the elastic element with sufficient power output for our requirements, geared electromotors are too heavy to directly mount on the exoskeleton. LOPES uses steel Bowden cables to connect external motors to the series elastic elements on the joints. The required cable pretension results in large amounts of nonlinear friction that fluctuates strongly with cable orientation changes due to exoskeleton movements. This friction is up to 40% of maximum torque. SEA can compensate for most friction but overall performance is still affected. An arm

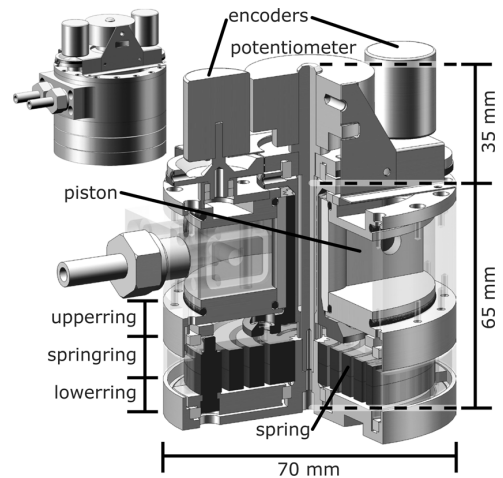


Fig. 2. rHEA, a rotational variant of the linear HEA [24], in a compact design [25], [26] for use on the Limbact exoskeleton. Open view from top to bottom: the angular sensors, the hydraulic actuator, and the spring.

exoskeleton has even larger joint rotations, resulting in more cable bending, and thus more and more unpredictable friction.

Therefore, for the SEA in the Limbact, the electromotors and Bowden cables were replaced with hydraulic actuation. The rotational hydraulic actuators and series elastic elements are mounted directly on the joints, but the heavy servo valves are not. These are placed on the base frame connected to the actuators via 2-m-long flexible tubes. Tube dynamics and other effects like piston friction are better predictable and much less variable with movement than the friction forces in Bowden cables. Any remaining unknown dynamic effects are accounted for by the aforementioned principles of SEA. The resulting rHEA is a rotational variant of the linear HEA [24].

The rHEA design (see Fig. 2) is a combination of a symmetric torsion spring, a rotational hydraulic actuator, and high-precision quadrature encoders. The overall design weighs less than 1.5 kg (including oil but excluding the weight of the flexible tubes), and has compact dimensions of 70×100 mm. The heaviest component, the steel spring, weighs 0.15 kg and is located at the bottom of the design. The lightest components, the sensors, are on the top.

The design has three rings in the bottom half. The upper ring is fixed to the upper half of the rHEA, which contains the housing of the hydraulic actuator and is connected to the base limb segment. The middle ring connects to the output of the hydraulic actuator and the inner ring of the spring. The lower ring connects to the outer ring of the spring and to the following limb segment. At the elbow, for instance, the upper ring is fixed to the upper arm and the lower ring to the forearm. The angular difference between the lower ring and the spring ring, times the spring stiffness, is the actuator torque. The spring deflection is limited to the maximum desired torque by a chamber in the lower ring. By manually locking the lower ring and spring ring together, the spring is bypassed and the rHEA can be used as a stiff hydraulic actuator. Locking all three rings together sets up the actuator for isometric measurements of up to 100 N·m, with the torque measured by strain gauges between the lower ring and the limb segment (not shown).

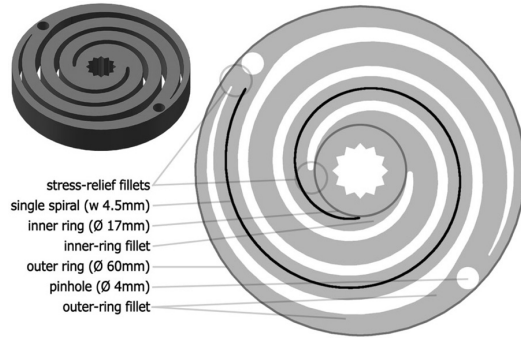


Fig. 3. Symmetric torsion spring from strong yet malleable maraging steel. The two windings cancel out each other's perpendicular endpoint forces. This keeps the spring center in the middle, and thereby reduces the load on bearings.

C. Symmetric Torsion Spring

The most important element in an SEA design is the elastic element. The spring stiffness should be chosen carefully; if too low, it reduces the torque bandwidth, and if too high, it increases the impedance and worsens the torque output resolution [18]. With recommendations from literature [24] and based on the experience with LOPES, a desired stiffness of about 150 N·m/rad was selected.

In another compact SEA design [25], [26], a spandrel-shape torsional spring with a stiffness of 327 N·m/rad was used. This long torsional spring ran through the center of their frameless motor and gearbox. The hydraulic actuator in the rHEA has no room for such a center spandrel, and for the desired compliance and torque resolution, their spring stiffness is too high. It is not trivial to lower the spring stiffness while maintaining strengths and dimensions.

To keep the design with the hydraulic actuator compact, the torsion spring needs to be flat like a clock spring. However, (un)wrapping a conventional clock spring results in offset forces at the spring center, and thus in large loads on the bearings and deformations in the construction. Using two symmetric windings cancels out their offsetting forces (see Fig. 3) at the cost of needing more material to achieve the same strength and spring stiffness. Maraging steel (type 18Ni, alloy 350) has a high yield stress of 2400 MPa and is very tough, resilient, and malleable, which are the desired properties for spring steel. With this steel, spring dimensions of 10-mm-high, 60-mm-diameter, and 4.5-mm-thick windings result in a spring with a maximum strength of 50 N·m and a spring stiffness of 150 N·m/rad. The Archimedean spiral of each winding starts at a inner radial distance of 8.5 mm and winds with a pitch of 12.6 mm for 1.35 revolutions. Fillets lower the stress on the spiral endings based on finite-element modeling. The springs were made by electrical discharge machining and chemical strengthening as instructed by the supplier.

Our finite-element program (COSMOSWorks, Dassault Systemes) did not calculate the large deformations and forces in the spring design correctly. Therefore, the initial spring used in the validation experiments later still had the old dimensions. This spring, with a 50-mm-diameter, 3.5-mm-thick winding and a 11.3-mm pitch, was a lot less stiff (88 N·m/rad) than originally intended. The windings touched each other at 22 N·m, long

before the desired maximum torque of 50 N·m. Visual observations learned that the oval deformation of the winding due to the torque load was much flatter in the real spring than predicted. After the validation experiments, further iterative steps led to the correct spring design as described earlier.

D. Sensors

In the rHEA, two ultraminiature, high-resolution quadrature kit encoders (Avago AEDA-3300 Series, $N_{ppr} = 80\,000$ pulses per revolution) measure the angle between the upper and lower rings, and between the upper and spring rings. The difference between the two encoders is equal to the deflection of the spring. By multiplying the deflection with the spring stiffness, the encoders function as a torque sensor with a maximum theoretical resolution equal to $2\pi K_{spr}/N_{ppr} \approx 0.01 \text{ N} \cdot \text{m}$, with K_{spr} being the spring stiffness.

The angle between the upper and lower rings is also measured by a potentiometer to initialize one of the encoders and signal any sensor malfunctions. Strain gauges between the lower ring and the exoskeleton (not shown) measure the spring torque. Divided by the spring stiffness, it should be equal to the deflection of the second encoder. The strain gauges thus have the same function as the potentiometer in encoder initialization and malfunction signaling. The strain gauges also measure the torque on the actuator during isometric experiments.

E. Control Model

An SEA controller manipulates the relative displacement of the spring. The original linear HEA used a standard proportional–integral (PI) controller [24]. The control diagram for the rHEA is similar (see Fig. 4) but has an additional feedforward gain K_{ff} parallel to the PI controller ($K_p + K_i/s$). The feedforward gain sets the opening of the hydraulic valve to get a known desired displacement for the spring. This prior knowledge results in less tracking error, enabling higher feedback gains of the PI controller and improving overall performance.

The following analysis is based on the HEA of Robinson and Pratt (2000, denoted later by “rp”) [24]. To get from their linear force-controlled HEA to our rotational torque-controlled rHEA, a few changes were needed. Each force F is replaced by torque T , displacement x by angle θ , and piston area A by piston area times the radius to the piston area center Ar ($A = 420 \text{ mm}^2$, $r = 16 \text{ mm}$). Tube dynamics H_{tube} and pressure feedback H_{pres} were added.

The original components of the generic control diagram [24], converted to the rotational actuator, are

$$H_{valve,rp}(s) = \frac{K_{v,rp}}{(\tau_1 s + 1)}$$

$$\text{or} \quad = \frac{K_{v,rp}}{(\tau_1 s + 1)(\tau_2 s + 1)(\tau_3 s + 1)}$$

$$H_{tube,rp}(s) = 1$$

$$H_{pist,rp}(s) = \frac{1}{Ar s}$$

$$H_{pres,rp}(s) = 0 \quad (1)$$

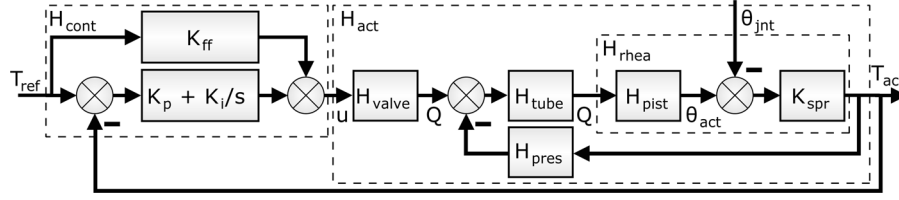


Fig. 4. rHEA control diagram. The controller H_{cont} uses feedforward gain K_{ff} and proportional and integrator gains K_p and K_i . H_{valve} represents the hydraulic valve, H_{tube} the tube dynamics of the 2-m-long flexible tubes, H_{pist} the rotational piston in the rHEA H_{rHEA} , and K_{spr} the rotational spring stiffness, which together form the complete actuator H_{act} . The actuator torque T_{act} is calculated by multiplying the deflection of the spring $(\theta_{\text{act}} - \theta_{\text{jnt}})$ with the spring stiffness K_{spr} .

in which H_{valve} is a first- or third-order approximation of the highly complex valve dynamics, converting a control signal opening the hydraulic valve u to a hydraulic flow Q based on the valve gain $K_{v,\text{rp}}$ and the time constants τ_{1-3} . The rotational piston H_{pist} in the rHEA displaces the spring by an angle θ_{act} based on the delayed incoming flow Q . After subtracting the joint displacement angle θ_{jnt} , the spring displacement is multiplied with the rotational spring stiffness K_{spr} .

The actuator model H_{act} was changed to account for some of the valve-flow dependency on the pressure drop caused by the increase of pressure feedback due to the deflected spring [24], [27], [28]

$$Q_{\text{max}} = K \sqrt{P_s - \frac{T_{\text{act}}}{Ar}} \quad (2)$$

by reducing the valve flow Q with a rough linearized gain approximation K_{pf} in the pressure feedback H_{pres} . As these effects were originally captured in the valve model $H_{\text{valve, rp}}$, this model was simplified to a direct gain. A transport delay H_{tube} was added that mimics the effects of the long tubes by delaying flow Q through the tubes by τ_2 . The components of the control diagram became

$$\begin{aligned} H_{\text{valve}}(s) &= K_v \\ H_{\text{tube}}(s) &= e^{-s\tau_2} \\ H_{\text{pist}}(s) &= \frac{1}{Ar s} \\ H_{\text{pres}}(s) &= \frac{K_{pf}}{Ar} \end{aligned} \quad (3)$$

The complete power chain H_{act} of valve, tube, and rHEA and the frequency response function (FRF) of the entire controlled system H_{sys} are given by

$$\begin{aligned} H_{\text{act}}(s) &= \frac{H_{\text{valve}} H_{\text{tube}} H_{\text{pist}} K_{\text{spr}}}{1 + (H_{\text{tube}} H_{\text{pist}} K_{\text{spr}} H_{\text{pres}})} \\ H_{\text{sys}}(s) &= \frac{(K_{ff} + K_p + (K_i/s)) H_{\text{act}}}{1 + (K_p + (K_i/s)) H_{\text{act}}} \end{aligned} \quad (4)$$

III. VALIDATION METHODS

The performance of the rHEA was validated with open- and close-loop multisine identification methods. For these experiments, a separate test setup was used in which the bottom (output) ring of the rHEA was connected to an external electromotor. The torque bandwidths of the rHEA were measured by giving it

multisine torque tracking tasks while keeping the external motor angle fixed. The rHEA's minimal impedance was determined by requiring it to maintain a zero-torque output during multisine angular disturbances of the external motor. Plotted results of step responses and virtual springs deflections demonstrate some time-domain properties of the rHEA. Finally, freeing the rHEA from the external motor allowed for manual interaction with hand and fingers.

A generic hydraulic pump and external accumulator delivered a constant source pressure P_s close to 8 MPa throughout the tests. The servo valve used was the Parker D1FP-E50M-9NS00 connected to flexible tubes rated for a maximum of 120 MPa and with a 6 mm inner diameter.

A. Multisine Identification

For the open- and closed-loop identifications, the system was perturbed with multisine input signals to estimate the frequency response $C(s)$ and squared coherence $\text{Coh}(s)$ functions. These functions were estimated with cross- and autospectral densities $S(s)$ of input (i) and output (o) [29], [30], [15]. For a black-box system with single-input-single-output, the functions are

$$\begin{aligned} C(s) &= \frac{S_{io}(s)}{S_{ii}(s)} \\ \text{Coh}(s)^2 &= \frac{|S_{io}(s)|^2}{S_{ii}(s) S_{oo}(s)} \end{aligned} \quad (5)$$

The FRF $C(s)$ is an estimate for the dynamics of the black-box system, and the squared coherence function $\text{Coh}(s)$ is a measure for the signal-to-noise ratio at each frequency. The squared coherence [31] ranges from zero to one, with zero meaning the lack of correlation between the input and output, and one meaning the absence of noise and time-varying behavior. Higher harmonics in periodic signals may still interfere with the interpretation of the coherence function.

For all but the minimal-impedance measurements, the input perturbation signal consisted of 80 summed sines with a observation time of 256 s. The frequencies of the sines were spaced logarithmically from 0.1 to 100 Hz, were of constant power spectral density, and had random phase shifts to reduce amplitude peaks in the summed signal. Due to the lack of the external motor power in the minimal-impedance measurements, this multisine input signal was limited to 64 sines, spaced from 0.1 to 25 Hz.

The logarithmical spacing of the sine frequencies prevented the use of crest optimization function on the input signal. Therefore, the amplitude of the total signal was scaled on two or three times the standard deviation and not the peak-to-peak values, with the mean of the signal always at zero. Measurements were repeated four times with four uniquely generated multisine signals differing on the used random phases. The results were averaged in the frequency domain over four frequencies and the four repetitions to improve the coherence of the measurements and estimates.

B. Open-Loop Actuator

For the open-loop identification of the rHEA ($H_{act,ol} = T_{act}/u$, where T_{act} is the rHEA output torque), the controller H_{cont} was disabled, the motor output angle θ_{jnt} fixed, and the valve opening signal u fed with a 0.1–100 Hz multisine (with three times the standard deviation equal to 5% valve opening). At 5%, the spring was at the end of its range of motion (equal to a maximum torque output of 22 N·m). Greater valve openings increased the rotational piston speed within the range of motion.

The identified FRF of the complete actuator $H_{act,ol}$ was fitted with the following models:

$$H_{act,ol1}(s) = \frac{K_{v,rp} K_{spr}}{(\tau_1 s + 1)s Ar} \quad (6)$$

$$H_{act,ol2}(s) = \frac{K_{v,rp} K_{spr}}{(\tau_1 s + 1)(\tau_2 s + 1)(\tau_3 s + 1)s Ar} \quad (7)$$

$$H_{act,ol3}(s) = \frac{K_{v,rp} K_{spr}}{(\tau_1 s + 1)s Ar} e^{-s\tau_2} \quad (8)$$

$$H_{act,ol4}(s) = \frac{K_v/K_{pf}}{(Ar/(K_{spr}K_{pf}e^{-s\tau_2}))s + 1}. \quad (9)$$

Of these, $H_{act,ol1}$ is the direct adaptation of the HEA actuator model [24] with a first-order valve model and without any additional tube dynamics. $H_{act,ol2}$ is the same but uses a third-order valve, also from the HEA [24]. $H_{act,ol3}$ follows directly from (4), and now includes a transport delay as model for the tube dynamics H_{tube} . $H_{act,ol4}$ is an adapted actuator model that uses the pressure feedback. It is the same as $H_{act,ol3}$ except for the pure integrator from the piston model H_{pist} , which is converted into a first-order system due to backpropagation of the pressure.

C. Closed-Loop Performance

To determine the closed-loop force bandwidth of the rHEA, the motor output angle θ_{jnt} was fixed and the controller H_{cont} had to track a 0.1–100 Hz multisine reference torque T_{ref} (with three times the standard deviation equal to 20 N·m). The closed-loop control gain settings were found using the Ziegler–Nichols tuning rules, with subsequent optimization of parameters based on the resulting closed-loop FRF. The force bandwidth of the rHEA was the lower of the –3 dB gain bandwidth and the 90 Hz phase-lag bandwidth of the FRF of the close-loop system $H_{sys,cl} = T_{act}/T_{ref}$, where T_{act} is the rHEA output torque.

To validate the correctness of the open-loop actuator model, the found best-fitting model (from $H_{act,ol1-4}$) was combined

with the system model H_{sys} . Using the closed-loop control gains, the theoretical system model H_{sys} was compared to the estimated closed-loop FRF $H_{sys,cl}$.

With the control gains known, the actuator can also be reverse estimated from the closed-loop identification $H_{sys,cl}$ by rewriting (4)

$$H_{act,cl}(s) = \frac{H_{sys,cl}}{(K_{ff} + K_p + (K_i/s)) - (K_p + (K_i/s))H_{sys,cl}}. \quad (10)$$

The FRFs of the actuator estimations $H_{act,cl05}$ and $H_{act,cl20}$ (estimated from the closed-loop FRFs at desired torque amplitudes of 5 and 20 N·m, respectively, at three times the standard deviation) were compared to the actuator $H_{act,ol}$ from the open-loop identification. The previously best-fitting open-loop model (from $H_{act,ol1-4}$) was fitted to both estimations.

Any differences found between the theoretical system model H_{sys} and the identified FRF of the system $H_{sys,cl}$, and the reverse estimation and identified FRF of the open-loop actuator indicate nonlinearities being present in the system.

For the minimal-impedance performance, the controller H_{cont} had to stay as close to the references torque T_{ref} of 0 N·m as possible, while the angular position θ_{jnt} was perturbed with a 0.1–25 Hz multisine with two times the standard deviation equal to 0.1 rad with the external electromotor. This electromotor was not capable of maintaining the constant power spectral density above 5 Hz, but the slight decay should not be a problem in (5).

D. Time-Domain Examples

The step responses and modeling of virtual springs illustrate the impedance-control performance of the actuator in the time domain. For the step responses, four different torque steps are repeated eight times per step size, with the angular output θ_{jnt} always fixed. For the virtual springs, the rHEA had to respond to an angular displacement θ_{jnt} as if it was a spring with a stiffness ranging from 5 to 200 N·m/rad. The angular displacement was realized by the external electromotor and consisted of a 1-Hz sine with a 0.1-rad amplitude.

IV. VALIDATION RESULTS

A. Open-Loop Actuator

The identified open-loop actuator and the four model fits are given in Fig. 5. The parameters for the fits of Fig. 5 are found in Table I, where K_{sys} is the system gain of each model. For $H_{act,ol4}$, τ_1 is the time constant of the equivalent first-order system.

The first two models ($H_{act,ol1-2}$) fit the data poorly. The low-frequency gain do not match, and the pure integrator in the transfer function keeps the low-frequency phase lag at 90°, while the identified actuator approaches 0°. They also do not match the high-frequency phase, at least not without significant distortion to the high-frequency gain. Adding a transport delay as the model for the tube dynamics H_{tube} does improve the fit on the high-frequency phase for $H_{act,ol3}$, but still does not match with the low-frequency gain and phase. Without the pure

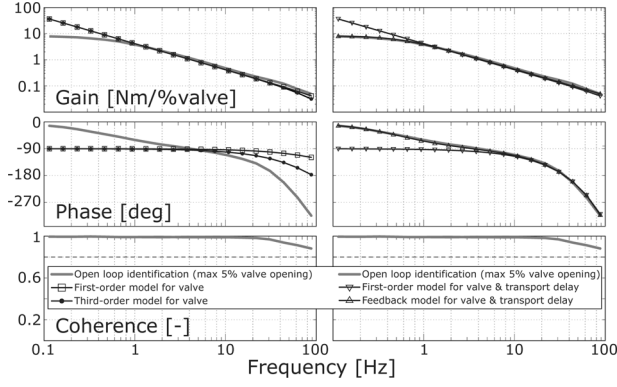


Fig. 5. Bode plot of the open-loop FRF of the complete actuator $H_{act,ol} = T_{act}/u$. The open-loop results were fitted with actuator models $H_{act,ol1-4}$ consisting of the valve, tube, piston, and spring components. $H_{act,ol1}$: line with open squares, $H_{act,ol2}$: line with closed circles, $H_{act,ol3}$: line with downwards pointing triangles, $H_{act,ol4}$: line with triangles pointing up. $H_{act,ol4}$ clearly results in the best fit.

TABLE I
PARAMETERS TO FIT MODELS $H_{act,ol1-4}$ TO IDENTIFIED $H_{act,ol}$ (FIG. 5)

	K_{sys}	τ_1	τ_2	τ_3
$H_{act,ol1}$	26	0.001	-	-
$H_{act,ol2}$	26	0.001	<0.001	<0.001
$H_{act,ol3}$	26	0.001	0.006	-
$H_{act,ol4}$	8.3	0.300	0.007	-

integrator in the transfer function, the pressure feedback model $H_{act,ol4}$ fits perfectly on the identified open-loop actuator.

B. Closed-Loop Performance

The identified FRF of the close-loop system $H_{sys,cl}$ has a -3 dB gain bandwidth of 35 Hz and a 90° phase-lag bandwidth of 18 Hz (see Fig. 6). The effects of the 2-m-long tubes between the hydraulic valve and the hydraulic actuator are seen in the rapidly increasing and unbound phase lag. The reduced coherence at the resonant peak is due to the spectral averaging over four frequencies there, which is of no concern.

The best-fitting actuator model ($H_{act,ol4}$) was combined with the system model H_{sys} . With the closed-loop control gains ($K_{ff} = 0.15$, $K_p = 1.85$, $K_i = 10$), the fit of the complete system $H_{sys,cl}$ was far from perfect, indicating the presence of nonlinearities as saturation in the actuator.

To investigate these nonlinearities, the open-loop identified $H_{act,ol}$ and closed-loop reverse-estimated actuators $H_{act,cl05}$ and $H_{act,cl20}$ were combined with the aforementioned control gains and compared and fitted with the best-fitting actuator model $H_{act,ol4}$ (see Fig. 7 and Table II). The behavior of the identified open-loop actuator and the closed-loop actuator at 5 N-m closely resembles each other. With the 20 N-m amplitude, the closed-loop actuator is significantly shifted in the gain and phase-lag plots, indicating the saturation and other nonlinearities of the valve-flow modeling in the actuator. The actuator model $H_{act,ol4}$ closely fitted all FRFs, except for the gain and phase-lag bumps at 30 Hz.

The minimal-impedance performance is given in Fig. 6. The expected leveling of the gain at the spring stiffness (88 N-m/rad for the experimental spring) at high frequencies

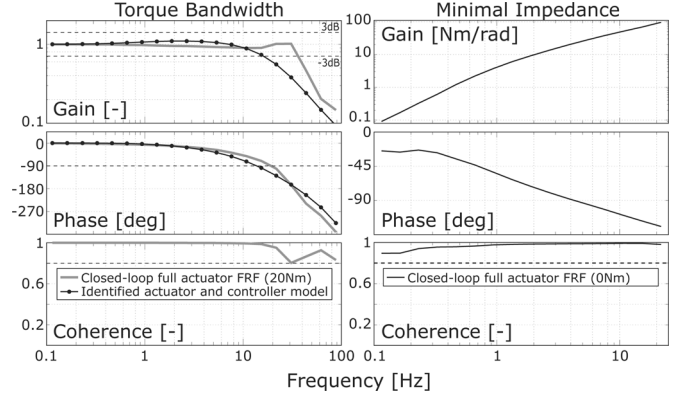


Fig. 6. Bode plots of the closed-loop force bandwidth (left) and minimal-impedance (right) measurements. (Left) The force bandwidth FRF $H_{sys,cl} = T_{act}/T_{ref}$ for the 20 N-m multisine reference torque (the gray line). When the best-fitting actuator model ($H_{act,ol4}$) was combined with the system model H_{sys} and the closed-loop control gains, the fit was far from perfect (line with filled circles). (Right) The minimal-impedance FRF $H_{img} = T_{act}/\theta_{jnt}$. For these measurements, the reference torque T_{ref} is 0 N-m, while the angular position θ_{jnt} was perturbed by a 0.1–25 Hz multisine with two times the standard deviation equal to 0.1 rad.

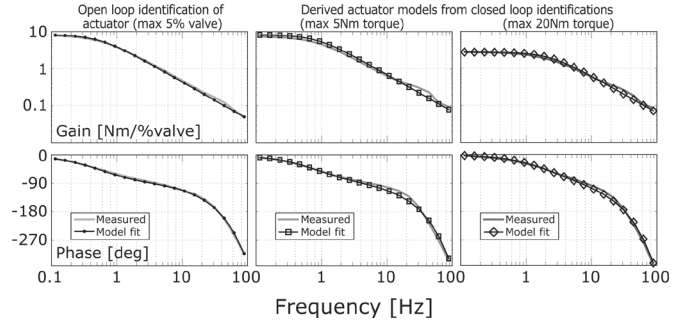


Fig. 7. Bode plot of the open-loop identified $H_{act,ol}$ and closed-loop estimated actuators $H_{act,cl05}$ and $H_{act,cl20}$. The behavior of the identified actuator (light gray line) and the closed loop estimated for the 5 N-m amplitude (gray line with closed circles) closely resembles each other. For the 20 N-m amplitude, the closed-loop actuator (dark gray line with open squares) is significantly shifted in the gain and phase-lag plots. For all identified actuators, the best-fitting actuator model $H_{act,ol4}$ fitted the data close to perfect.

TABLE II
PARAMETERS TO FIT MODEL $H_{act,ol4}$ TO IDENTIFIED $H_{act,ol}$, $H_{act,cl05}$, AND $H_{act,cl20}$ (FIG. 7)

	K_{system}	τ_1	τ_2
$H_{act,ol}$	8.3	0.30	0.0070
$H_{act,cl05}$	8.3	0.19	0.0075
$H_{act,cl20}$	2.6	0.07	0.0080

was not achieved, as the external motor could not reach these frequencies. Theoretically, the leveling for this stiffness should start at roughly 25 Hz, above which only the physical spring characteristics of SEA are felt.

C. Time-Domain Examples

The step responses are given in Fig. 8. Overshoot and response time are all acceptable for rehabilitation purposes, although using a better inverse model for the feedforward control H_{ff} —as opposed to the current linear gain K_{ff} in Fig. 4—may further improve the results. The variability of the response overshoot

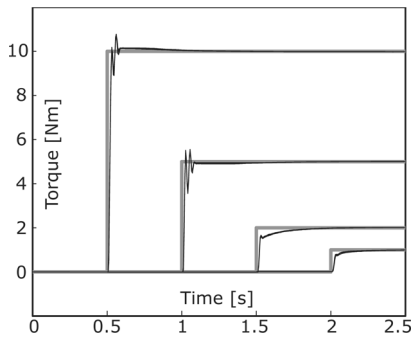


Fig. 8. Time plots of step reference signals. Gray: the required torque T_{ref} ; black: the measured torques T_{act} .

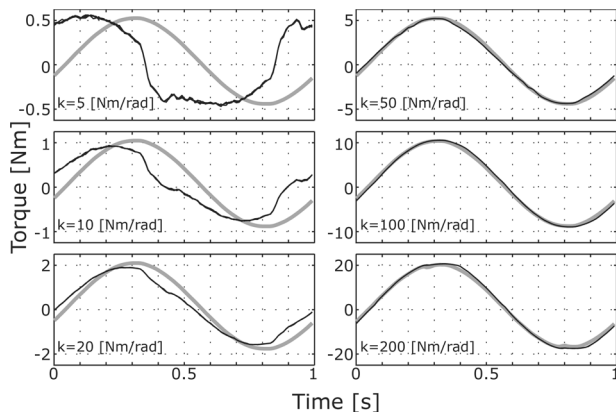


Fig. 9. Time plots of virtual springs. The external motor maintained a 1-Hz sine with a 0.1-rad amplitude on the angular position θ_{jnt} , while the virtual spring stiffness was increased from 5 to 200 N-m/rad. (Note the real spring stiffness of 88 N-m/rad.) The gray lines are the measured joint angles θ_{jnt} multiplied by the virtual spring stiffness, resulting in the desired torque signal T_{ref} . The recorded actuator torques are plotted in black.

and settling time indicates that nonlinearities are present in the physical rHEA.

The behavior of the virtual springs is given in Fig. 9. Based on these results and experimental experience, the minimal stiffness was limited by the minimal output torque required and not necessarily the lowness of the virtual stiffness. Below 1 N-m, even though the controller could realize the required output torque resolution, it also generates phase lead, probably because of unaccounted valve and tube dynamics and piston friction. The 200 N-m/rad upper limit of the virtual spring stiffness was the result of the maximum actuator torque T_{act} of 22 N-m and the 0.1 rad reference amplitude. Increasing the first or lowering the second makes higher virtual spring stiffness possible, although a system with high virtual stiffness might need an input filter to ensure stable operations at every frequency [22].

V. DISCUSSION AND CONCLUSION

The rHEA combines a compact and relatively lightweight design with the strength and power of hydraulics and the back-drivability and compliance of SEA. With the validation experiments, both the design requirements and the modeling accuracy were investigated.

A. Design

The most novel feature in the rHEA design is a custom-designed, compact, symmetric torsion spring machined out of high-strength maraging steel. This series elastic element could potentially be scaled (not tested) and used for all kinds of SEA. It is thus not necessarily restricted to combinations with hydraulic actuation or for the torque dimensions detailed here. In general, the thicker the winding or the overall spring, the higher the allowable torque and the stiffer the spring will be. Longer windings reduce the spring stiffness, but need more room to wrap and unwrap. Best results are achieved when the windings just touch when the maximum torque is reached, as this acts as an integrated safety mechanism to reduce overstretching of the outside of the windings. Other non-Archimedean spirals, for instance, exponential spirals, were not explored, but may result in a better displacement profile.

The original torsion spring as used in the experiments did not reach the desired maximum torque of 50 N-m and was with 88 N-m/rad weaker than expected. After the validation experiments, an iterative approach resulted in a spring for the rHEA with the desired 50 N-m of maximum output torque and 150 N-m/rad of spring stiffness. The bandwidth performance of this latter spring will be slightly better due to the higher stiffness. Therefore, as found with the original spring, the multisine torque bandwidth of at least 18 Hz, the theoretical maximum torque measurement resolution of 0.01 N-m (not validated experimentally), and the torque output resolution of less than 1 N-m are more than acceptable. The weight of the final rHEA is 1.3 kg below the desired maximum of 1.5 kg. Also, when the minimal impedance and modeled virtual springs were manipulated by manually rotating the actuator output ring, almost no torque distortion was felt.

By manually locking the spring ring to the output ring, the rHEA can also operate as a stiff hydraulic actuator. When locking all three rings, it becomes an isometric measurement device. A stiff hydraulic actuator in admittance control can achieve more precise and faster position perturbations as compared to impedance control of SEA.

Compared to other actuators, the rHEA has all the advantages and disadvantages of SEA as described in Section I. Furthermore, the power density is higher compared to pneumatic actuators [32] and electromotors (with or without a series elastic element [25], [26]) due to the use of hydraulic actuation [33]. Compared to direct hydraulic actuators, the series elastic element makes the rHEA more compliant and patient friendly. Finally, compared to the Bowden cable configuration of the LOPES SEA [20], the rHEA has a smoother torque output and is less sensitive to bending of the cable. However, the power needed for impairment quantifications may cause safety issues for rehabilitation therapy, and using hydraulics may be less desirable in clinical settings due to the required pumps, noise issues, and possible hydraulic leakage.

B. Modeling

The HEA model of Robinson and Pratt [24] was modified, which resulted in a better fit to the measured open-loop FRF of

the actuator. A transport delay was added to the original model to recreate the observed time lag in the FRF, which improved the high-frequency fit. But only when a rough approximation of pressure feedback was added to the actuator model—in effect remove the pure integrator from the transfer function—did the modified model give an almost perfect fit to the gain and phase lag at both high and low frequencies. Comparison to the original study [24] is difficult, as the fit of the open-loop actuator they showed did not include frequency responses below 2 Hz. Based on what can be seen, the modified model may better fit their actuator measurements too as: 1) their low-frequency phase response seems to start with less than 90° phase lag and 2) their phase lag at high frequency keeps on dropping, where their third-order valve model and pure system integrator should level out at 360° . We speculate that more realistic and nonlinear valve-flow functions based on both pressure drop over the valve and the valve opening [see (2)] might result in better future models.

C. Conclusions

In conclusion, the rHEA was found to be suitable for rehabilitation therapy and impairment quantification of the upper extremities. It had the desired bandwidths, resolution, and amplitude ranges, while the design was kept light and compact. The rHEA will be mounted on the new exoskeleton, the Limpact (see Fig. 1).

REFERENCES

- [1] J. van der Lee, I. Snels, H. Beckerman, G. Lankhorst, R. Wagenaar, and L. Bouter, "Exercise therapy for arm function in stroke patients: A systematic review of randomized controlled trials," *Clin. Rehabil.*, vol. 15, no. 1, pp. 20–31, 2001.
- [2] T. Platz, "Evidence-based arm rehabilitation—A systematic review of the literature," *Nervenarzt*, vol. 74, no. 10, pp. 841–849, 2003.
- [3] G. Prange, M. Jannink, C. Groothuis-Oudshoorn, H. Hermens, and M. IJzerman, "Systematic review of the effect of robot-aided therapy on recovery of the hemiparetic arm after stroke," *J. Rehabil. Res. Dev.*, vol. 43, no. 2, pp. 171–184, 2006.
- [4] G. Kwakkel, B. Kollen, and H. Krebs, "Effects of robot-assisted therapy on upper limb recovery after stroke: A systematic review," *Neurorehabil. Neural Repair*, vol. 22, no. 2, pp. 111–121, 2008.
- [5] R. Schmidt and T. Lee, *Motor Control and Learning*, 3rd ed. Champaign, IL: Human Kinetics, 1999.
- [6] G. Kwakkel, R. Wagenaar, J. Twisk, G. Lankhorst, and J. Koetsier, "Intensity of leg and arm training after primary middle-cerebral-artery stroke: A randomised trial," *Lancet*, vol. 354, no. 9174, pp. 191–196, 1999.
- [7] S. Barreca, S. Wolf, S. Fasoli, and R. Bohannon, "Treatment interventions for the paretic upper limb of stroke survivors: A critical review," *Neurorehabil. Neural Repair*, vol. 17, no. 4, pp. 220–226, 2003.
- [8] H. Feys, W. De Weerd, G. Verbeke, G. Steck, C. Capiat, C. Kiekens, E. Dejaeger, G. Van Hoydonck, G. Vermeersch, and P. Cras, "Early and repetitive stimulation of the arm can substantially improve the long-term outcome after stroke: A 5-year follow-up study of a randomized trial," *Stroke*, vol. 35, no. 4, pp. 924–929, 2004.
- [9] J. Liu, S. Cramer, and D. Reinkensmeyer, "Learning to perform a new movement with robotic assistance: Comparison of haptic guidance and visual demonstration," *J. Neuroeng. Rehabil.*, vol. 3, p. 20, 2006.
- [10] A. Stienen, E. Hekman, F. van der Helm, G. Prange, M. Jannink, A. Aalsma, and H. van der Kooij, "Freebal: Dedicated gravity compensation for the upper extremities," presented at the 10th ICORR 2007, Noordwijk, The Netherlands, Jun. 13–15.
- [11] A. Stienen, E. Hekman, F. van der Helm, G. Prange, M. Jannink, A. Aalsma, and H. van der Kooij, "Dampace: Dynamic force-coordination trainer for the upper extremities," presented at the 10th ICORR 2007, Noordwijk, The Netherlands, Jun. 13–15.
- [12] E. Wolbrecht, V. Chan, D. Reinkensmeyer, and J. Bobrow, "Optimizing compliant, model-based robotic assistance to promote neurorehabilitation," *IEEE Trans. Neural Syst. Rehabil. Eng.*, vol. 16, no. 3, pp. 286–297, Jun. 2008.
- [13] T. Nef, M. Mihelj, and R. Riener, "ARMin: A robot for patient-cooperative arm therapy," *Med. Biol. Eng. Comput.*, vol. 45, no. 9, pp. 887–900, 2007.
- [14] E. J. Perreault, R. F. Kirsch, and A. M. Acosta, "Multiple-input, multiple-output system identification for characterization of limb stiffness dynamics," *Biol. Cybern.*, vol. 80, no. 5, pp. 327–337, 1999.
- [15] F. van der Helm, A. Schouten, E. de Vlugt, and G. Broun, "Identification of intrinsic and reflexive components of human arm dynamics during postural control," *J. Neurosci. Methods*, vol. 119, no. 1, pp. 1–14, 2002.
- [16] A. Schouten, E. de Vlugt, J. van Hilten, and F. van der Helm, "Quantifying proprioceptive reflexes during position control of the human arm," *IEEE Trans. Biomed. Eng.*, vol. 55, no. 1, pp. 311–321, Jan. 2008.
- [17] J. Veneman, R. Kruidhof, E. Hekman, R. Ekkelenkamp, E. van Asseldonk, and H. van der Kooij, "Design and evaluation of the lopes exoskeleton robot for interactive gait rehabilitation," *IEEE Trans. Neural Syst. Rehabil. Eng.*, vol. 15, no. 3, pp. 379–386, Sep. 2007.
- [18] G. Pratt and M. Williamson, "Series elastic actuators," in *Proc. IROS 1995*, Aug. 5–9, pp. 399–406.
- [19] D. Robinson, "Design and analysis of series elasticity in closed-loop actuator force control" Ph.D. dissertation, Massachusetts Inst. Technol. (MIT), Cambridge, 2000.
- [20] J. Veneman, R. Ekkelenkamp, R. Kruidhof, F. van der Helm, and H. van der Kooij, "A series elastic- and Bowden-cable-based actuation system for use as torque actuator in exoskeleton-type robots," *Int. J. Robot Res.*, vol. 25, no. 3, pp. 261–281, 2006.
- [21] R. Ekkelenkamp, P. Veltink, S. Stramigioli, and H. van der Kooij, "Evaluation of a virtual model control for the selective support of gait functions using an exoskeleton," in *Proc. IEEE 10th Int. Conf. Rehabil. Robot. (ICORR 2007)*, Noordwijk, The Netherlands, Jun. 13–15, pp. 693–699.
- [22] H. Vallery, J. Veneman, E. van Asseldonk, R. Ekkelenkamp, and H. M. Buss van der Kooij, "Compliant actuation of rehabilitation robots: Benefits and limitations of series elastic actuators," *IEEE Robot. Autom. Mag.*, vol. 15, no. 3, pp. 60–69, Sep. 2008.
- [23] A. Stienen, E. Hekman, H. ter Braak, A. Aalsma, F. van der Helm, and H. van der Kooij, "Rotational hydro elastic actuator for a torque driven exoskeleton for the upper-extremities," presented at the Biorob 2008, Scottsdale, AZ, Oct. 19–22.
- [24] D. Robinson and G. Pratt, "Force controllable hydro-elastic actuator," in *Proc. ICRA 2000*, vol. 2, pp. 1321–1327.
- [25] J. Sensinger and R. Weir, "Unconstrained impedance control using a compact series elastic actuator," in *Proc. 2nd MESA 2006*, Beijing, China, Aug. 13–16, pp. 1–6.
- [26] J. Sensinger and R. Weir, "User-modulated impedance control of a prosthetic elbow in unconstrained, perturbed motion," *IEEE Trans. Bio-Med. Eng.*, vol. 55, no. 3, pp. 1043–1055, Mar. 2008.
- [27] J. Heintze, G. van Schothorst, A. van der Weiden, and P. Teerhuis, "Modeling and control of an industrial hydraulic rotary vaneactuator," in *Proc. 32nd Conf. Decis. Control*, San Antonio, TX, Dec. 15–17, 1993, pp. 1913–1918.
- [28] A. Alleyne and R. Liu, "A simplified approach to force control for electro-hydraulic systems," *Control Eng. Practice*, vol. 8, no. 12, pp. 1347–1356, 2000.
- [29] G. Jenkins and D. Watts, *Spectral Analysis and Its Applications*. San Francisco, CA: Holden Day, 1969.
- [30] J. Bendat and A. Piersol, *Random Data: Analysis and Measurement Procedures*. New York: Wiley, 1986.
- [31] R. Pintelon and J. Schoukens, *System Identification: A Frequency Domain Approach*. New York: IEEE Press, 2001.
- [32] H. Van der Kooij, J. Veneman, and R. Ekkelenkamp, "Compliant actuation of exoskeletons," in *Mobile Robotics—Towards New Applications*. Mammendorf, Germany: Verlag Rober Mayer-Scholz, 2006.
- [33] J. Huber, N. Fleck, and M. Ashby, "The selection of mechanical actuators based on performance indices," *Proc. R. Soc. A*, vol. 453, no. 1965, pp. 2185–2205, 1997.

Authors' photographs and biographies not available at the time of publication.